The Thesis Committee for Gregory Burg
Certifies that this is the approved version of the following Thesis:

Resonant Tunneling in Double Bilayer Graphene – WSe_2 Heterostructures

APPROVED BY
SUPERVISING COMMITTEE:

Emanuel Tutuc, Supervisor

L. Frank Register

Resonant Tunneling in Double Bilayer Graphene – WSe_2 Heterostructures

by

Gregory Burg

Thesis

Presented to the Faculty of the Graduate School of

The University of Texas at Austin

in Partial Fulfillment

of the Requirements

for the Degree of

Master of Science in Engineering

The University of Texas at Austin

December 2018

Acknowledgements

Although I am the sole author of this work, many individuals provided significant contributions, both directly and indirectly, to the methods and results discussed herein. First, I would like to thank my advisor, Prof. Emanuel Tutuc, for his endless support and guidance throughout my research career thus far. In particular, his immense help in contriving experiments and interpreting data, without which I would not be able to claim the experimental accomplishments that I do now, as well as his continued and principled encouragement to make me a better researcher.

I would also like to thank the senior-most members of my group, who never hesitated to offer help in any situation: Stefano Larentis, who first showed me the ropes of fabrication in the cleanroom and was a constant source of both knowledge and humor; Kyoung Kim, who was a bottomless source of guidance for anything fabrication related; Hema Movva, whose breadth and depth of knowledge in seemingly all fields related to solid state electronics was truly remarkable and invaluable; and Babak Fallahazad, who sat one desk over from me and thus bore the brunt of my numerous questions as a fledgling researcher, answering every one patiently and with incredible knowledge and experience.

I also thank the theorists who have provided vital interpretations and context to my experimental data: Nitin Prasad, who created the tunneling model presented in this work and was always available for discussions; Amithraj Valsaraj, who did the band structure modeling for this work; and Prof. L. Frank Register, who guided the previously mentioned students in their work, always provided key insights into difficult to understand experimental results, and kindly agreed to be a reader for this thesis.

I must also thank the people, both in my group and outside it, who are always up for a friendly discussion, scientific or otherwise, and make research at MRC an enjoyable experience, day in and day out: Feng Wen, Yimeng Wang, David Villareal, Michael Rodder, Amritesh Rai, Atresh Sanne, Tanuj Trivedi, Mir Mohammad Sadeghi, and many others.

I thank the MRC staff who make my research possible: Ricardo Garcia, Jesse James, Bill Ostler, Christine Wood, Jean Toll, Gerlinde Sehne, Joyce Kokes, Darren Robbins, and James Hitzfelder.

And finally I thank my parents, Mary and Greg, my brother, Gardner, and my girlfriend, Monica, for their love and support, and their willingness to listen to both my frustrations and success stories alike.

Abstract

Resonant Tunneling in Double Bilayer Graphene – WSe_2 Heterostructures

Gregory Burg, MSE

The University of Texas at Austin, 2018

Supervisor: Emanuel Tutuc

We demonstrate gate-tunable resonant tunneling and negative differential resistance between two rotationally aligned bilayer graphene sheets separated by bilayer WSe_2. We observe large interlayer current densities of 2 $\mu A/\mu m^2$ and 2.5 $\mu A/\mu m^2$, and peak-to-valley ratios approaching 4 and 6 at room temperature and 1.5 K, respectively, values that are comparable to epitaxially grown resonant tunneling heterostructures. An excellent agreement between theoretical calculations using a Lorentzian spectral function for the two-dimensional (2D) quasiparticle states, and the experimental data indicates that the interlayer current stems primarily from energy and in-plane momentum conserving 2D-2D tunneling, with minimal contributions from inelastic or non-momentum conserving tunneling. We demonstrate narrow tunneling resonances with intrinsic half-widths of 4 and 6 meV at 1.5 K and 300 K, respectively.

Table of Contents

List of Tables

List of Figures

Chapter 1: Introduction

The recent emergence of two-dimensional (2D) materials, such as graphene, hexagonal boron-nitride (hBN) and transition metal dichalcogenides (TMDs), coupled with advancing fabrication techniques for stacking 2D materials, has opened numerous pathways to explore the electronic and photonic properties, and device applications of van der Waals (vdW) heterostructures.[1] Evolving techniques for the layer-by-layer transfer of 2D materials allow for great flexibility in device structure, and have led to the study of many interesting phenomena in van der Waals heterostructures, such as quantum Hall effect[2] and moiré bands[3–6] in high mobility graphene on hBN substrates, quantum Hall effect in TMDs encapsulated in hBN[7,8], and resonant tunneling in double monolayer or double bilayer graphene separated by hBN.[9–14] The latter phenomenon requires the conservation of both electron energy and momentum in tunneling between two independently contacted 2D layers, and leads to interlayer current-voltage characteristics with gate-tunable negative differential resistance (NDR).[15]

One of the challenges in realizing functional vdW heterostructures using layer-by-layer transfers is the control of atomic registration between adjacent layers, and in particular that of rotational alignment, which is necessary for an efficient coupling between layers. In contrast to epitaxially grown heterostructures, where rotational alignment is ensured by the atomic bonding of successive layers, in vdW heterostructures of 2D materials the relative rotational alignment of different layers is most often not controlled. Because resonant tunneling requires a precise overlap of states in momentum space, and desirably a strong interlayer coupling, it serves as a powerful tool to probe the quantum fingerprints of vertical transport in vdW heterostructures. Furthermore, the gate-tunable NDR of the interlayer current-voltage characteristics enable the implementation of novel

interlayer tunneling field-effect transistors (ITFETs), with potential applications for both Boolean and non-Boolean logic.[16–18]

This work outlines the underlying physics, device fabrication, electrical characterization and theoretical modeling of gate-tunable resonant tunneling with large interlayer conductance and negative differential resistance between two highly rotationally aligned bilayer graphene flakes separated by bilayer WSe_2. Chapter 2 provides an introduction to two dimensional crystals and their electronic properties, and affirms 2D materials as an ideal platform to probe energy and momentum conserving tunneling in vertical heterostructures. Chapter 3 details the fabrication techniques and processes that enable the creation of heterostructures with precise lateral and rotational alignment of the constituent layers while maintaining high quality interfaces. In Chapter 4 we employ four-point measurements to probe the intrinsic tunneling current-voltage characteristics independent of the contact resistance, which becomes relevant in our samples due to the large interlayer conductance. We observe current densities of 2 $\mu A/\mu m^2$ at room temperature, and 2.5 $\mu A/\mu m^2$ at 1.5 K, as well as NDR with peak-to-valley ratios (PVRs) up to 4 and 6 at room temperature and 1.5 K, respectively, which are comparable to values measured in epitaxially grown resonant tunneling heterostructures. Chapter 5 shows calculations of the tunneling current as a function of interlayer and gate bias that are in very good agreement with the measured tunneling current at all biasing conditions, using a simple perturbative Hamiltonian model with Lorentzian broadening of the 2D quasiparticle states. This agreement indicates the measured tunneling is energy and momentum conserving, and therefore coherent with respect to the single particle states.

Chapter 2: Resonant Tunneling in 2D Materials

2D MATERIALS

Two-dimensional (2D) materials are a class of layered materials characterized by strong in-plane covalent bonding, and weak out-of-plane van der Waals bonding.[1] This bond strength anisotropy allows for the isolation of atomically thin sheets from bulk crystals using micromechanical cleavage techniques. The most well-known 2D material is graphene, a monolayer hexagonal lattice of carbon atoms derived from graphite, which was first isolated in 2004.[19] Graphene is a semi-metal with conduction and valence bands forming Dirac cones at the corners (**K**-points) of its hexagonal Brillouin zone. The linear dispersion at low energies gives rise to massless charge carriers which, coupled with extremely low defect densities, produces large mobilities, exemplified by the observation of the integer[20] and fractional[21] quantum Hall effects in high quality samples. Another key characteristic of graphene is its low density of states, which enables direct tuning of its Fermi level by electrically gating the layer. In this work, we focus on bilayer graphene, which is also a semi-metal with band minima at the **K**-points, but with a parabolic low-energy dispersion. The bilayer graphene band structure opens a band gap at the **K**-point through the application of a transverse electric field.[22]

Alongside graphene is a large collection of 2D materials with finite bandgaps. The most prevalent is a group of semiconductors in the transition metal dichalcogenide family, which take the chemical form MX_2, where M is either molybdenum or tungsten and X is one of sulfur, selenium, or tellurium. In the 2*H* phase, a TMD monolayer consists of a sheet of M atoms sandwiched between two sheets of X atoms in the trigonal prismatic form, as shown in Figure 2.1. TMDs have a number of layer (thickness) dependent band gap that ranges from ~1-2 eV and an indirect to direct band gap transition at the monolayer limit.[23]

Such characteristics make TMDs promising candidates for optical and optoelectronic applications, although electronic performance is limited by low mobilities at room temperature.[23] We concentrate here on bilayer WSe_2, which has an indirect band gap of ~1.8 eV between the **Γ** (valence band maximum) and **K** (conduction band minimum) points, and a slightly large direct gap at the **K**-point. WSe_2 flakes of sufficiently high quality have been shown to exhibit the quantum Hall effect.[7]

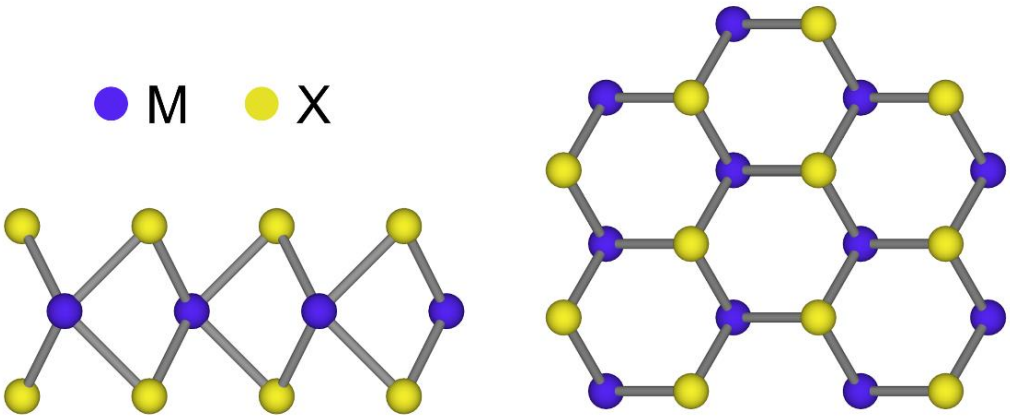

Figure 2.1: TMD crystal structure. Side (left) and top (right) view of a TMD monolayer crystal lattice. Transition metal (M) atoms are sandwiched between top and bottom chalcogen (X) atoms in a trigonal prismatic geometry.

Finally, hexagonal boron nitride is an insulating 2D materials with a band gap of 5.8 eV.[24] hBN has a hexagonal crystal structure, similar to graphene, with each boron atom bonding to three nitrogen atoms. The surface of hBN is atomically smooth, making it an ideal substrate and gate dielectric in 2D heterostructures. In comparison to an SiO_2 substrate, samples prepared on hBN show significantly reduced surface roughness scattering and improved mobility.[2]

ENERGY AND MOMENTUM CONSERVING TUNNELING

Due to the weak nature of van der Waals bonding, 2D materials can be stacked to form heterostructures with minimal strain on the layers from lattice mismatch. This inherently makes 2D materials a more flexible platform for junction and band engineering relative to traditional epitaxial heterostructures, as demonstrated by 2D based p-n junctions[25,26], photovoltaic devices[27,28], and vertical tunneling field effect transistors.[10,11,29,30] In this work, we consider a specific type of vertical tunneling in which carriers conserve energy and in-plane momentum, known as resonant tunneling.[31] The resonant tunneling heterostructures described here consist of two rotationally aligned bilayer graphene layers, separated by a bilayer WSe_2 barrier layer and encapsulated in ~20 nm top and bottom hBN.

To achieve resonant tunneling, the graphene crystals must be rotationally aligned in order to align their Brillouin zones in momentum space (Figure 2.2a), which allows electrons to tunnel between the **K**-points of the two layers while conserving momentum. However, rotational alignment is only a prerequisite for energy and momentum conserving tunneling. For resonant tunneling current to flow between layers in a rotationally aligned system, there must be filled states in one layer that can tunnel into corresponding empty states in the opposite layer at the same energy and momentum. This condition is dependent on the *energetic* alignment of the layer band structures, as controlled by interlayer and gate biases.

The biasing conditions at which resonant tunneling occurs can be understood by examining the band structures of each layer and their dependence on an applied gate and interlayer bias. Figure 2.2c shows the band diagram of a resonant tunneling heterostructure for a positive gate voltage, and zero interlayer voltage. While the Fermi levels μ_{TL} and μ_{BL} of the top and bottom layer, respectively, are aligned, the applied gate bias induces different

charge densities in each layer, leading to a finite electrostatic potential difference V_{ES} = (ϕ_{BL} - ϕ_{TL})/e between layers, which suppresses energy and momentum conserving tunneling; here e is the electron charge and ϕ_{BL} and ϕ_{TL} are the energies of the charge neutrality points (band minima) of the top and bottom layers, respectively. On the other hand, an appropriate interlayer bias restores V_{ES} = 0 V (Figure 2.2d), and allows for energy and momentum conserving tunneling, leading to a maximum in the interlayer current. Experimentally, this can be observed by setting the gate voltage and sweeping the interlayer voltage in order to find the resonant condition, marked by a peak in the interlayer current.

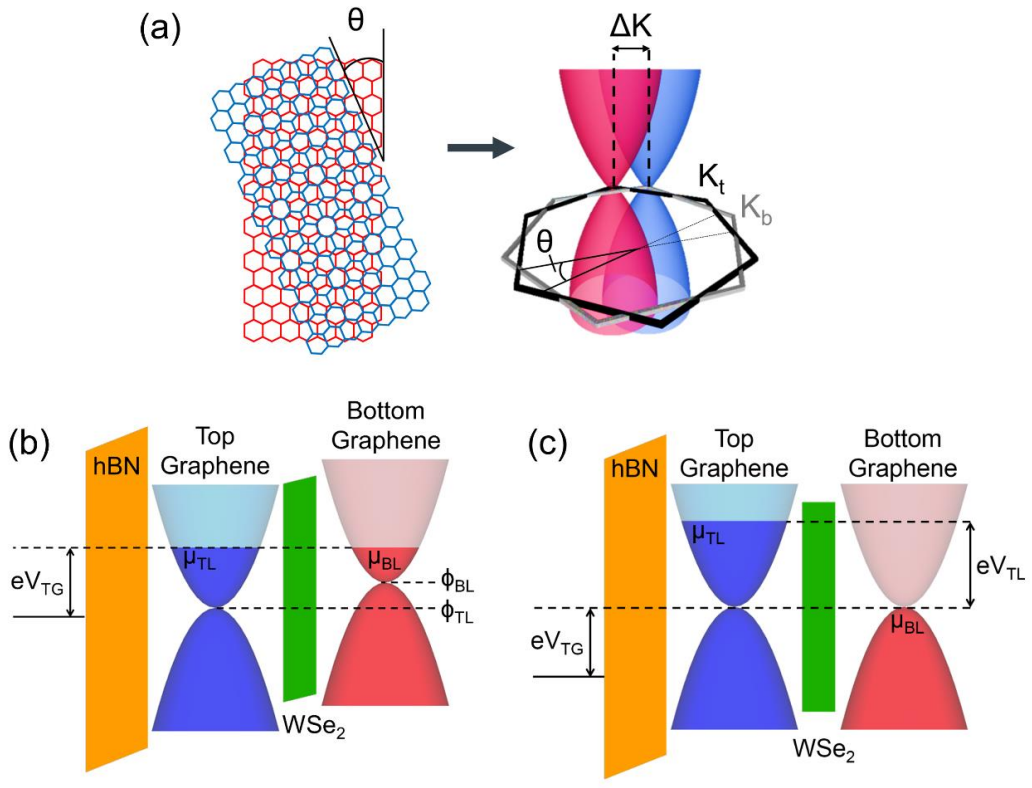

Figure 2.2: Band alignments in resonant tunneling heterostructures. (a) A rotational misalignment of the graphene crystals (left) leads to a corresponding misalignment of the

Brilllouin zones in momentum space (right), which creates a momentum displacement ($\Delta\mathbf{K}$) between the layer band structure at their respective **K**-points, preventing momentum conservation in tunneling. (b, c) Simplified energy band diagrams of the resonant tunneling heterostructure at (b) a positive gate bias (V_{TG}) and zero interlayer bias, and (c) aligned charge neutrality points at the same gate bias and an appropriate finite interlayer bias (V_{TL}).

Chapter 3: Fabrication of Resonant Tunneling Heterostructures

DRY TRANSFERS

All heterostructures investigated here are fabricated using a layer-by-layer dry transfer technique, in which a viscoelastic stamp is used to pick up and stack layers one-by-one. The stamp consists of a thick rectangular polydimethylsiloxane (PDMS) substrate with a hemispherical protrusion in the center. The hemisphere is made by placing a small enough droplet of liquid PDMS onto the substrate that no outward flow occurs and allowing it cure. Before a transfer, a thin layer of polypropylene carbonate (PPC) is placed onto the stamp by spin coating PPC dissolved in anisole at 3000 rpm and baking at 180° C to remove the solvent. The hemispherical geometry of the stamp limits the size of the contact area between the stamp and the substrate to a circle approximately 150 μm in diameter. This dramatically improves the selectivity of layer pick-up relative to a planar geometry, which contacts the substrate everywhere, and allows for closely spaced layers on the same substrate to be picked up in separate steps.

A modified mask aligner is used to perform layer transfers. The stamp is adhered to a glass slide, inverted, and held in place by the vacuum mask holder of the aligner. The substrate that the target 2D flake will be picked up from is placed on a vacuum chuck below the stamp. A microscope above the setup looks through the transparent stamp onto the substrate and is used to identify the target flake. X and Y micromanipulators then position the flake in line with the hemispherical stamp, before a Z micromanipulator is used to raise the substrate until contact with the stamp is made. A resistive heating element sits underneath the substrate and sets the temperature of the target flake during the transfer using a temperature controller. Figure 3.1 shows a schematic of the described transfer setup.

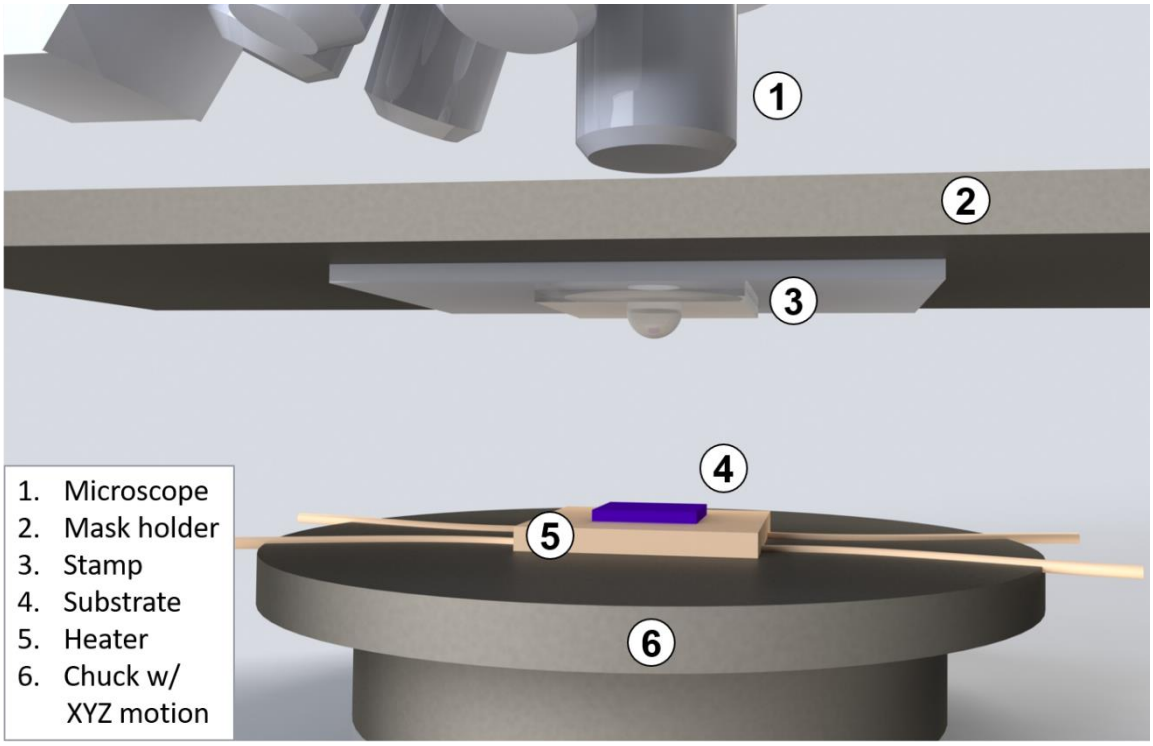

Figure 3.1: Schematic of the setup used to perform dry transfers of 2D materials

When the stamp is brought into contact with a flake at ~45° C, the PPC adheres strongly enough to the flake to overcome the flake's adhesion to the substrate, and can pick the flake up upon quickly lowering the substrate. The flake can then be released from the stamp onto a new substrate by bringing the two into contact and increasing the temperature to above the glass transition temperature of PPC, approximately 80° C, then slowly lowering the substrate. During fabrication of a heterostructure, the stamp only makes direct contact with the top hBN as described above. For all subsequent layers, the van der Waals attraction between layers is used to pick up the next layer, as illustrated in Figure 3.2.

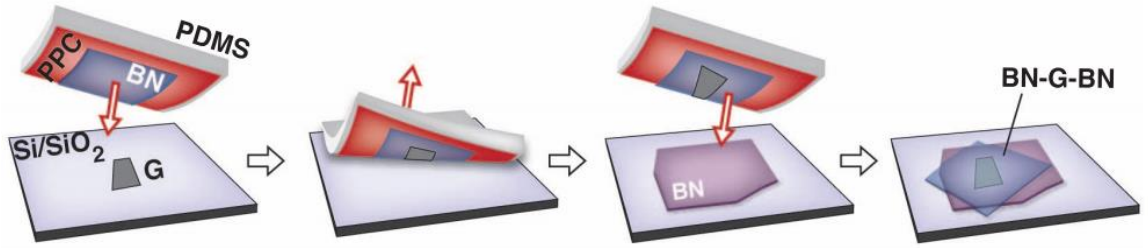

Figure 3.2: (from Reference 32) Dry transfer of multilayer structures. After picking up the top hBN directly with PPC, the next layer can be picked up through van der Waals interaction with the hBN while avoiding direct polymer contact. This can be repeated for all layers in the heterostructure before releasing onto the bottom hBN.

FABRICATION FLOW

The fabrication flow of a resonant tunneling heterostructure is as follows: first, graphene, WSe_2, and hBN multilayers are mechanically separated using tape and exfoliated onto separate Si/SiO_2 substrates. Bilayer graphene flakes then are identified using optical microscopy and Raman spectroscopy. The full width half maximum (FWHM) of the 2D peak in the graphene Raman spectrum increases as a function of the flake thickness and can be used to conclusively determine the number of layers.[33] For bilayer graphene, the FWHM of the 2D peak is approximately 51 cm^{-1}, as shown in Figure 3.3a. Large area graphene flakes are required because both the top and bottom graphene layers in the heterostructure will originate from the same initial flake to ensure rotational alignment.

For bilayer WSe_2, flakes are first identified optically based on color and contrast, before performing photoluminescence measurements to confirm the thickness. Here, the position and intensity of the direct and indirect gap peaks in the photoluminescence spectrum uniquely identify the number of layers.[34] Furthermore, the intensity of the peaks in the spectrum are an indication of flake quality, with higher quality flakes showing a stronger signal than lower quality flakes. Figure 3.3b shows a typical photoluminescence

spectrum for bilayer WSe_2, which is characterized by two closely spaced peaks of similar intensity.

Finally, hBN flakes are chosen based on size, thickness, and surface roughness. The flakes must be large enough to fully cover the encapsulated active layers, the thickness determines the capacitance of the hBN as a gate dielectric, and the smoothness of the flake directly affects the mobility of the active layers on top of it. After optical identification, atomic force microscopy is used to determine the thickness and surface roughness of the hBN flake with sub-nanometer accuracy.

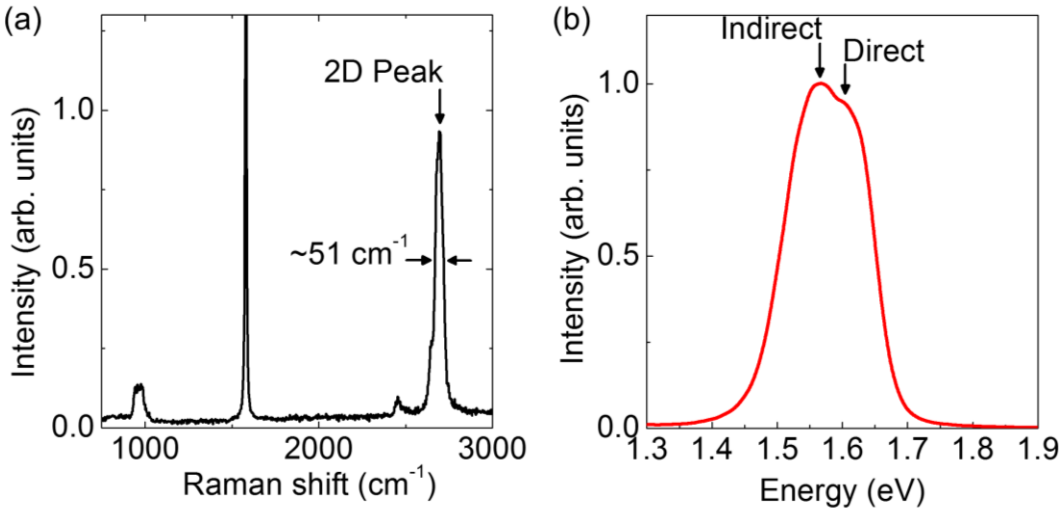

Figure 3.3: Graphene and WSe_2 layer thickness characterization. (a) Typical Raman spectrum of a bilayer graphene flake. The FWHM of the 2D peak identifies the number of layers. (b) Typical photoluminescence spectrum of a WSe_2 bilayer. The closely spaced peaks corresponding to the direct and indirect gaps indicate a bilayer.

After identifying the desired bilayer graphene, WSe_2, and hBN flakes, the first processing step is to define the top and bottom graphene layers using electron beam lithography (EBL) and oxygen plasma etching. A spacing of at least 20 μm between the two layers is needed when picking up one layer to prevent the stamp from contacting the

other layer and introducing unwanted residue to the active tunneling area. A side effect of the etching process is an increased adhesion of the graphene to the SiO_2 substrate, which prevents the graphene from being picked up easily by the top hBN. In order to pick up the graphene, the hBN is first released from the stamp onto the graphene, and the layers are annealed for one hour at 380° C in ultra-high vacuum. The two layers can then be picked up together reliably. Next, the interlayer WSe_2 is picked-up using the top hBN and graphene layers before dropping the heterostructure onto the bottom graphene layer, annealing and picking up again as described above.

In parallel with the above processing, a Cr/Pt electrode is defined, using EBL and e-beam metal evaporation, onto an empty substrate to serve as a back gate. The bottom hBN layer is then transferred onto the metal and multiple Cr/Pd electrodes are defined on the hBN, which will make independent, metallic contacts to the top and bottom graphene layers. After each of these steps, the sample is annealed for three hours at 390° C to remove any residues from EBL resist or PPC. The upper portion of the heterostructure is then transferred onto the bottom hBN and metal contacts and annealed for two hours at 380° C to clean the layer interfaces and improve adhesion between layers. Then, a Cr/Pd/Au top gate is evaporated onto the top hBN, as well as large pads connected to the layer contacts. Finally, the sample is glued and wire bonded to a dual inline package (DIP) header so that it can be seated into a DIP socket for electrical characterization utilizing all the independent electrodes. Figure 3.4 shows a typical heterostructure throughout the described fabrication steps.

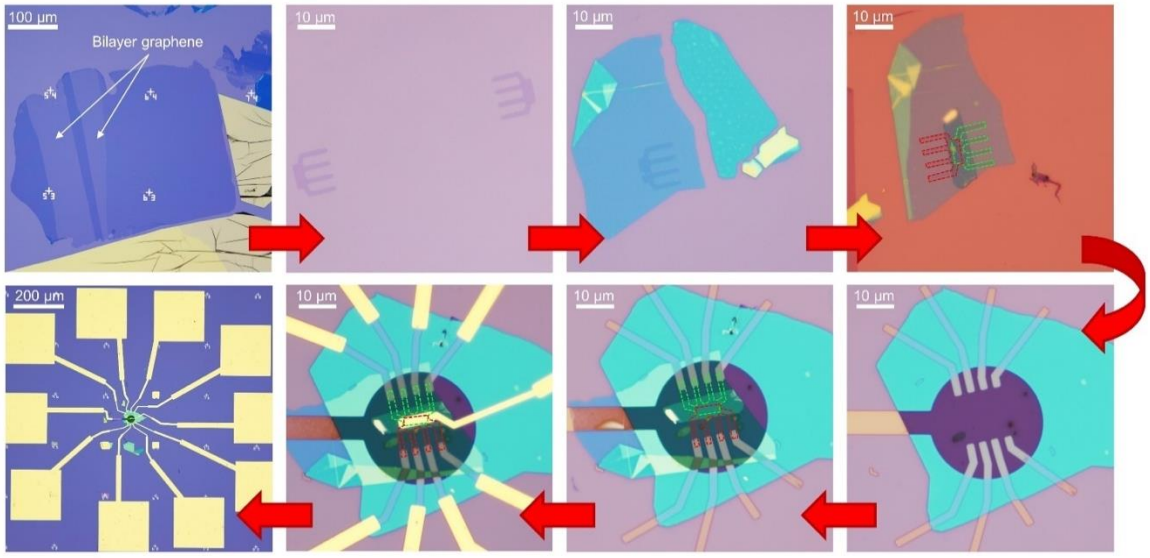

Figure 3.4: Fabrication flow of a resonant tunneling heterostructure. First, a large area bilayer graphene flake is exfoliated. Then, the graphene is etched to form the top and bottom graphene layers. Next, the top hBN is picked up (not shown) and released onto the top graphene layer. The interlayer WSe_2 is then picked up using the top hBN/graphene stack (not shown) and dropped onto the bottom graphene layer. In parallel the bottom gate, bottom hBN, and bottom contacts are prepared. The upper heterostructure is then dropped onto the bottom substrate. Finally, the top gate and large pads are deposited. The top (green) and bottom (red) bilayer graphene layers are outlined in some panels for better visibility.

Chapter 4: Electrical Characteristics of Resonant Tunneling Heterostructures

BACKGROUND

Previous studies of resonant tunneling between two 2D layers in vdW heterostructures have used either double monolayer graphene or double bilayer graphene separated by hBN.[9–14] For these samples, rotational alignment was achieved by either using the graphene flakes straight edges to identify principal crystal axes, and subsequently aligning them during transfer[10–12], or by using two mono- or bilayer graphene that stem from a single crystal domain, and are therefore rotationally aligned at the outset.[13] The use of bilayer graphene[12,13], or multilayer graphene[35], leads to narrower resonance thanks to reduced impact of the quantum capacitance. Two main drawbacks of these device designs limit applications for high speed digital electronics, and implementation beyond prototyping, desirable at wafer scale. First, the use of large bandgap hBN[24] as an interlayer dielectric reduces the interlayer current density and conductance. For example, a four-monolayer thick interlayer hBN translates into a specific interlayer conductance of ~10 nS/μm^2 at small interlayer bias, corresponding to an RC time constant of 10^{-6} s for a capacitance C = 1.8 μF/cm^2.[13] Second, the growth of large area hBN by chemical vapor deposition has so far resulted in lower crystal quality relative to exfoliated hBN, limiting its scalability.[36,37] While graphene double layers separated by a TMD have been reported, these samples did not show resonant tunneling[30], and the coupling of the two graphene layers through the TMD could not be assessed.

The use of WSe_2 as an interlayer tunnel barrier is attractive for several reasons. First, with a bulk and monolayer bandgap of approximately 1.2 eV[38] and 2 eV[39], respectively, WSe_2 is a smaller bandgap alternative to the 5.8 eV[24] gap in hBN, resulting in larger tunneling currents. Additionally, WSe_2 can be isolated down to mono- or few-

layer thick single crystals of high quality[40], which is crucial for minimizing defect induced scattering of tunneling carriers. Finally, it has been shown that in heterostructures with graphene, the mid-gap of WSe_2 is close to the neutrality point of graphene.[41]

DEVICE STRUCTURE

Figure 4.1a shows a schematic of the interlayer tunneling field-effect transistor (ITFET) studied here, consisting of two individually contacted bilayer graphene flakes separated by bilayer WSe_2. The samples are realized using a series of dry transfers,[32] and are encapsulated with hBN as top and bottom dielectrics. The bilayer graphene flakes originate from a larger area single-crystal and remain aligned to within 0.1 degrees during the transfers, which ensures a close alignment of their crystal axes in the final heterostructure.[13] We note that it has been shown that when brought into close alignment, 2D crystals can adjust themselves to achieve perfect alignment, so it is possible the alignment accuracy is better than that stated above.[6] Photoluminescence (PL) spectroscopy confirms the WSe_2 thickness.[34] Multiple contacts to each layer are defined by e-beam lithography, plasma etching, and metal deposition, which enables a decoupling of the contact resistance in vertical tunneling measurements.

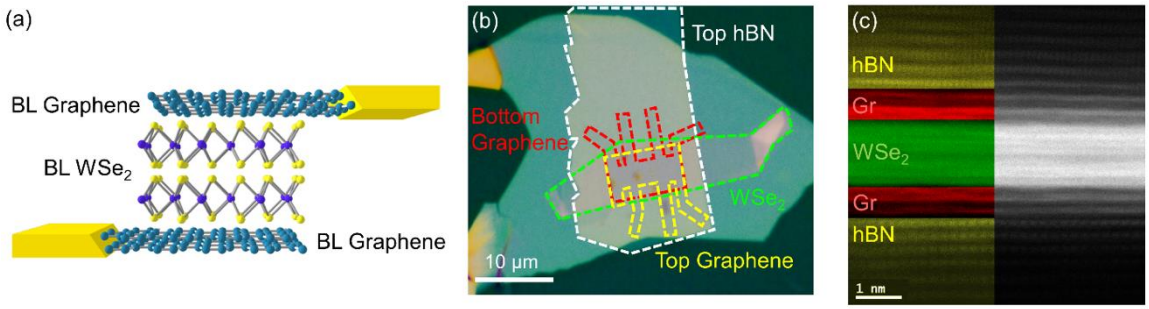

Figure 4.1: Double bilayer graphene separated by bilayer WSe_2 interlayer tunneling field-

effect transistor. (a) Schematic representation of the device structure, including independent contacts to bilayer graphene channels. (b) Optical micrograph of a completed heterostructure. The dashed lines indicate individual layers. (c) Cross-sectional STEM of a double bilayer graphene ITFET separated by WSe_2 and encapsulated in hBN dielectric. The individual layers are identified using EELS and EDS.

Figure 4.1b shows an optical micrograph of one double bilayer graphene heterostructure separated by WSe_2 and encapsulated in hBN, with the contour of each layer marked. Figure 4.1c shows a scanning transmission electron micrograph (STEM) of the heterostructure, demonstrating atomically clean interfaces. Electron energy loss spectroscopy (EELS) and energy dispersive X-ray spectroscopy (EDS) are used to identify the different atomic layers in the heterostructure. While multiple heterostructures were fabricated for this study, we focus here on two specific double bilayer graphene heterostructures separated by bilayer WSe_2, labelled as Device #1 and Device #2.

TWO-POINT ELECTRICAL CHARACTERIZATION

Tunneling heterostructures are characterized at room temperature in a vacuum probe station that has been modified to measure samples wire bonded to DIPs. The DIP is placed into a socket, which is fed into a breakout box through which every electrical contact to the heterostructure can be probed independently or in conjunction with other contacts. A Stanford Research Systems lock-in amplifier is used to measure resistances at constant, small currents. Typically, this instrument is used to measure the contact resistance at the interface of the bilayer graphene and Cr/Pd contacts. An Agilent 4156C semiconductor parameter analyzer is used to measure the current-voltage characteristics of the heterostructures. This instrument utilizes source monitor units to simultaneously sweep

voltage and measure current in a single probe, as well as voltage monitor units to measure voltage (i.e. for a four-point measurement).

Cryogenic electrical characterization is carried out in a pumped helium variable temperature insert (VTI), with a base temperature of 1.5 K. The DIP is mounted to a socket on a probe that is lowered into the VTI. Like the setup described above, the heterostructure is probed using lock-in amplifiers and a parameter analyzer. Additionally, the cryostat houses a superconducting magnet that can be swept up to 14 T, for measurements of tunneling in the presence a magnetic field.

We probe the tunneling current-voltage characteristics by measuring the interlayer tunneling current (I_{int}) as a function of the interlayer bias (V_{TL}) applied to the top layer, while the bottom is grounded (Figure 4.2b inset), at different top gate voltages (V_{TG}), and back gate voltage V_{BG} = 0 V. The top and bottom hBN dielectrics have thicknesses of 14 nm and 31 nm, respectively. For hBN's dielectric constant of 3, the top and back gate capacitances are C_{TG} = 190 nF/cm^2 and C_{BG} = 86 nF/cm^2, using $C = k(\varepsilon_0/t)$, where k is the material dependent dielectric constant, ε_0 is the vacuum permittivity and t is the layer thickness. Figure 4.2a shows I_{int} vs. V_{TL} measured at different V_{TG} values in Device #1 at room temperature. The data show clear NDR that is V_{TG} dependent, with a maximum areal current density J_{int} = 2 μA/μm^2, and PVR of 3.9. Interestingly, the current peaks are followed by discontinuous drops for all V_{TG} values, a pattern that differs markedly from previously observed NDR in double layers separated by hBN, where the tunneling current has a continuous dependence on interlayer bias.[9–13] In addition, the current densities are approximately one order of magnitude larger than values corresponding to the same interlayer thickness in the best performing double layer heterostructures using hBN as the interlayer dielectric.[10] Figure 4.2b shows the I_{int} vs. V_{TL} data measured at different V_{TG} in

the same device at a temperature T = 1.5 K. Figure 4.2b data is very similar to Figure 4.2a data, except for a slight increase in the peak current in each trace.

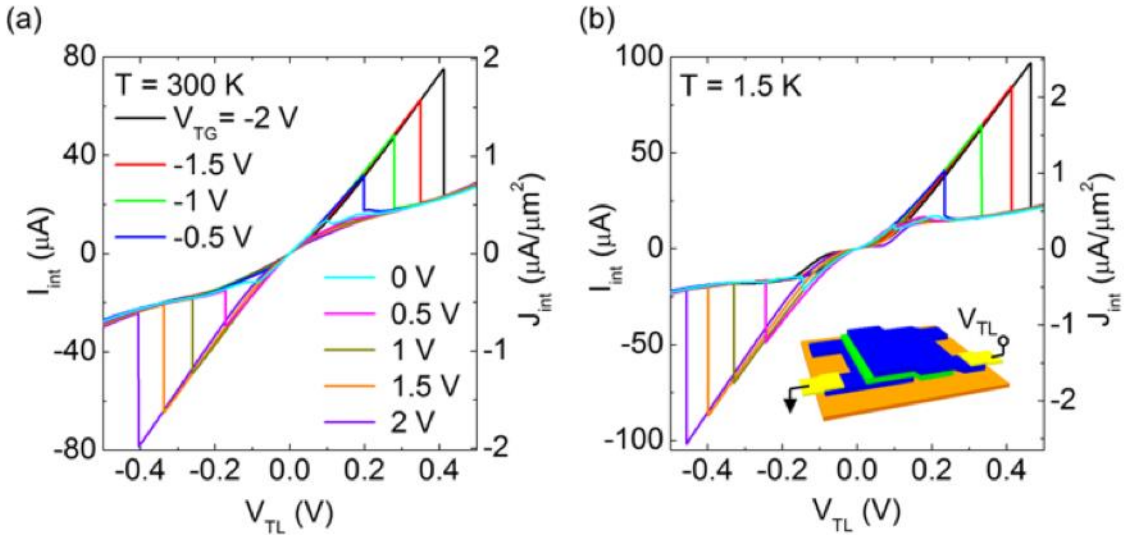

Figure 4.2: Resonant tunneling in double bilayer graphene ITFET. (a, b) Two-point I_{int} vs. V_{TL} at different V_{TG}, measured at (a) T = 300 K, and (b) T = 1.5 K in Device #1. The right axes of (a) and (b) show I_{int} normalized to the bilayer graphene overlap area. Panel (b) inset shows a schematic of the interlayer biasing setup.

To understand the discontinuity in the I_{int} vs. V_{TL}, we consider the role of an external (contact) resistance in series with the interlayer tunneling resistance. The external resistance has contributions from both the metal/graphene contact resistance, and the in-plane resistance of the bilayer graphene extensions outside the overlap area. Considering these external contributions is important in our devices, because Figure 4.2a shows a maximum current of 80 μA at V_{TL} = 0.4 V, corresponding to a total device resistance of 5 kΩ, a value comparable to that of single layer graphene field-effect transistors with similar dimensions.[32] As such, a non-negligible fraction of V_{TL} drops across the contacts and bilayer graphene extensions, reducing the voltage across the tunnel barrier.

We can explicitly take into account the contact resistance (R_c) by expressing the applied external voltage as $V_{TL} = \Delta V + I_{int}R_c$, where ΔV is the voltage drop across the WSe_2 tunnel barrier. The I_{int} value is controlled by the band alignment between layers, and therefore by ΔV, but it must also satisfy the above equation, which can be rewritten as:

$$I_{\mathrm{int}} = \frac{V_{\mathrm{TL}} - \Delta V}{R_{\mathrm{c}}} \tag{4.1}$$

To illustrate the impact of external resistance in NDR devices, in Figure 4.3a we show a generic I_{int} vs. ΔV curve with NDR. At a given V_{TL}, Equation 3.1 is a linear function in the same graph with a slope of $-1/R_c$ and x-intercept of V_{TL}, referred to as a load line. At a fixed V_{TL}, the measured I_{int} is determined by the intersection of the load line with the intrinsic tunneling I_{int} vs. ΔV characteristic. Figure 4.3a shows three representative load lines, Cases 1 – 3. As V_{TL} is increased from 0 V, the load line intersects I_{int} vs. ΔV at a single point in Case 1. At a sufficiently high V_{TL}, as for Cases 2 and 3, the load line will intersect the I_{int} vs. ΔV data at multiple points, and the measured I_{int} is determined by the V_{TL} sweep history. Specifically, for load lines between Cases 2 and 3 the measured I_{int} will be determined by the lowest (highest) ΔV intersection point if V_{TL} is swept upward (downward). This will lead to a sharp I_{int} drop as the load line transitions from multiple to one intersection point with the I_{int} vs. ΔV data, namely at Case 3 on the V_{TL} up-sweep, and at Case 2 on the V_{TL} down-sweep, and hysteresis. Additionally, different portions of the I_{int} vs. ΔV are sampled depending on the V_{TL} sweep direction, as indicated in Figure 4.3a.

Figure 4.3b shows calculated I_{int} vs. V_{TL} characteristics using Figure 4.3a I_{int} vs. ΔV data, for different R_c values. While all traces exhibit NDR, as the contact resistance is increased, the I_{int} vs. V_{TL} are "stretched" towards higher voltages, with sections of positive

(negative) slope becoming elongated (compressed). Beyond a critical R_c value, the load line begins to intersect the NDR region at multiple points, and discontinuities in I_{int} accompanied by hysteresis are observed. In this regime, a subset (grey section in Fig. S1a) of the I_{int} vs. ΔV trace cannot be accessed experimentally. Figure 4.3a shows the same behavior observed experimentally in Device #2, where a tunable external series resistance (R_{ext}) is used to recreate the effect. We note that compared to Device #1, the contact resistance of the heterostructure in Figure 4.3c is smaller than the tunneling resistance in the NDR region, and as such does not lead to hysteresis and abrupt jumps in the current-voltage characteristics at $R_{ext} = 0$.

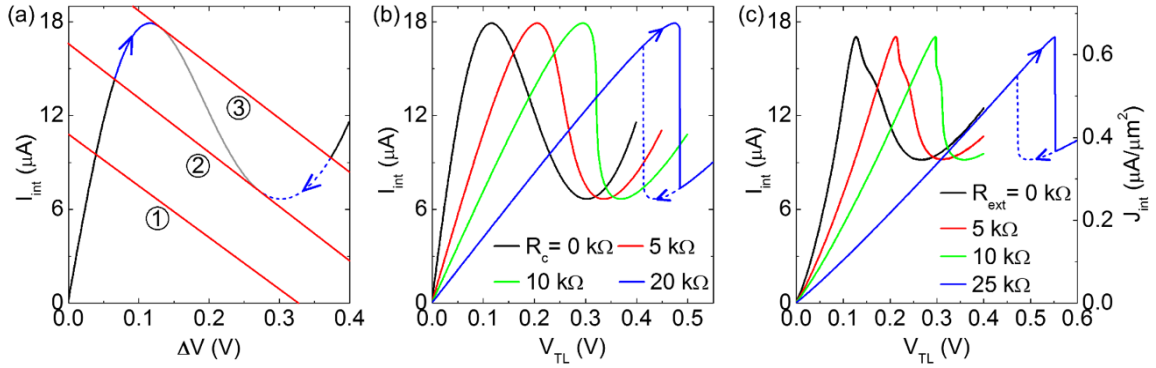

Figure 4.3: Impact of series resistance on the measured characteristics of NDR devices. (a) Generic I_{int} vs. ΔV characteristic with NDR, along with load lines (red) corresponding to different applied V_{TL}. At a given V_{TL}, the intersection of the load line with the I_{int} vs. ΔV curve determines the measured current. In regions with one intersection point (Case 1), the measured current is independent of the external voltage sweep direction (black). In regions with multiple intersection points (Cases 2 and 3), the measured current depends on the external voltage sweep direction. The solid (dashed) blue line marks the section of the I_{int} vs. ΔV probed on the external voltage up-sweep (down-sweep). For a given series resistance, a subsection of the I_{int} vs. ΔV characteristic (grey) cannot be probed. (b) I_{int} vs. V_{TL} calculated using panel (a) data for different R_c values. (c) Experimentally measured I_{int} vs. V_{TL} for Device #2, in series with a tunable R_{ext}.

FOUR-POINT ELECTRICAL CHARACTERIZATION

In light of these findings, a key question is what are the intrinsic ITFET tunneling characteristics, and how to experimentally separate these characteristics from contact resistance effects. To address this question, we performed four-point tunneling measurements where an additional pair of contacts measure the voltage across the tunnel barrier (ΔV), which excludes the voltage dropped across the contacts (Figure 4.4b inset). Figure 4.4a shows I_{int} vs. ΔV measured at various V_{TG} values and at room temperature in Device #1. Compared to Figure 4.2 data, the resonance peaks are much sharper and appear at lower voltages relative to the two point measurements. Furthermore, consistent with the prior discussion, the sections of I_{int} vs. ΔV data that show NDR are experimentally inaccessible as a result of finite R_c.

Figure 4.4b shows I_{int} vs. ΔV measured at different V_{TG} values, and at T = 1.5 K. Compared to the room temperature data of Figure 4.4a, the peak (background) I_{int} increase (decrease) only slightly while the peak positions are unchanged, suggesting that neither phonon scattering nor thermionic emission play a dominant role in the tunneling. Figure 4.4c illustrates the weak temperature dependence of I_{int} vs. ΔV data at V_{TG} = 0 V. Figure 4.4d shows the intrinsic differential conductance (g_{int}) vs. ΔV at different T, calculated from the Figure 4.4c data. The data shows narrow conductance peaks associated with the resonant tunneling, with full width at half maximums ranging from ~8 mV at T = 1.5 K to 20 mV at T = 300 K. The inset of Figure 4.4d displays a close-up of the conductance peaks of the Figure 4.4c main panel. The apparent splitting of the conductance peak at T = 1.5 K is likely associated with a small band gap opening in one of the two bilayers.[22] The sharp peaks in both the four-point interlayer current and differential conductance indicate a high degree of rotational alignment between layers, and suggest a high quality heterostructure with contaminant-free interfaces.

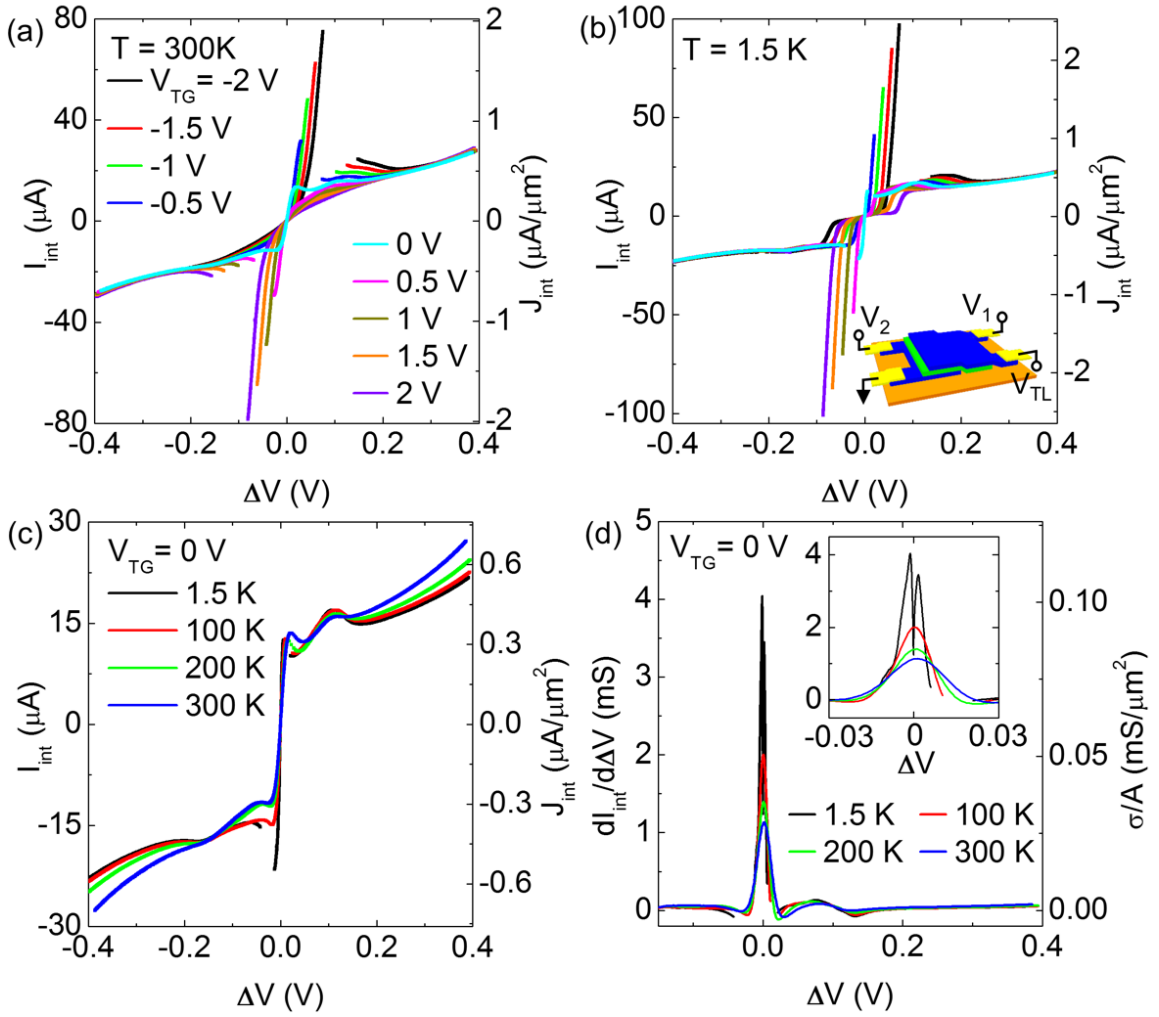

Figure 4.4: Intrinsic tunneling current-voltage characteristics. (a, b) Four-point I_{int} vs. ΔV at different V_{TG}, measured at (a) T = 300 K, and (b) T = 1.5 K in Device #1. Panel (b) inset shows a schematic of the interlayer biasing setup. (c) Four-point I_{int} vs. ΔV at V_{TG} = 0 V and at different T values. The right axes of (a - c) show I_{int} normalized to the bilayer graphene overlap area. (d) g_{int} vs. ΔV corresponding to panel (c) data. The right axis shows g_{int} normalized to the overlap area (A). Inset: close-up of the conductance peaks near ΔV = 0.

To further confirm that the observed I_{int} peaks are a result of the relative band alignments between the two graphene layers, and are driven by momentum conserving tunneling, we apply an in-plane magnetic field during tunneling measurements. The

magnetic field does not influence carrier transport within each layer, but during tunneling it will provide an additional momentum component to the electrons via the Lorentz force, which has the net effect of translating the band structure of one layer relative to the other in momentum space (Figure 4.5b), similar to a rotational misalignment of the layers. Therefore, an increasing in-plane magnetic field should reduce the amplitude of the resonance peak, as the bands shift away from each other and the number of momentum conserving tunneling states decreases. Figure 4.5c shows magneto-tunneling measurements that follow the expected behavior and confirm that the resonance peak does stem from momentum conserving tunneling. We note that the resonance peak is not fully extinguished by a magnetic field of 14 T, indicating that the resulting momentum shift of the band structures is smaller than the energy broadening of the tunneling states.

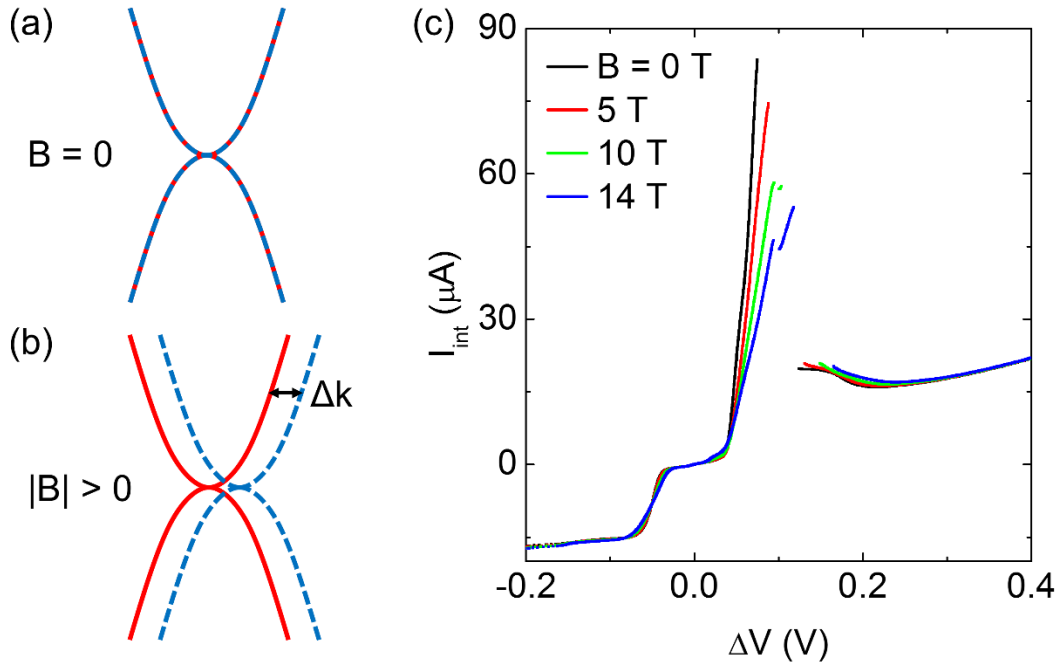

Figure 4.5: Resonant tunneling in an in-plane magnetic field (*B*). (a) Top (dashed blue) and bottom (solid red) layer band structures aligned at the resonance condition for zero magnetic field. (b) The same biasing condition as (a) but with an in-plane magnetic field that displaces the top layer relative to the bottom layer in momentum space by Δk. (c)

Experimental I_{int} vs. ΔV for various B values, showing a marked decrease in the resonance peak with increasing magnetic field.

COMPARISON TO EPITAXIAL HETEROSTRUCTURES

It is informative to compare the device characteristics of the double bilayer graphene separated by WSe_2 heterostructure to other resonant tunneling vdW and epitaxial heterostructures. We consider J_{int}, ΔV, the specific conductance at the resonance peak, the PVR, operating temperature, and whether or not the NDR is gate-tunable as the main metrics characterizing resonant tunneling devices. Our device characteristics are comparable to many epitaxially grown heterostructures.[42–52] While some epitaxial heterostructures show a larger PVR, they typically have a lower peak specific conductance[43,46,47,50,52], and gate-tunable NDR was demonstrated only in GaAs/AlGaAs double quantum wells at temperatures lower than 170 K.[47,48] In addition, the heterostructure described here outperforms previous vdW heterostructures employing an hBN interlayer dielectric.[9–11,13] A summary of these metrics for various epitaxial and vdW heterostructures is shown in Table 4.1.

heterostructure	*peak J_{int} ($\mu A/\mu m^2$)*	*peak ΔV (V)*	*peak cond. ($mS/\mu m^2$)*	*PVR*	*operating temp.*	*gate-tunable*	*ref. no.*
AlGaAs/GaAs	67	0.65	0.103	3.9	300 K	No	42
AlGaAs/GaAs	86	0.9	0.096	14.3	77 K	No	42
InAs/AlSb/GaSb	0.35	0.05	0.007	20	300 K	No	43
InAs/AlSb/GaSb	1.05	0.05	0.021	88	77 K	No	43
InGaAs/AlAs/InAs	75	0.9	0.083	42	300 K	No	44
InAs/AlSb	7300	1.25	5.840	3.3	300 K	No	45
InGaAs/InAlAs	2	0.4	0.005	104	300 K	No	46

GaAs/AlGaAs	1.0×10^{-4}	0.015	6.7×10^{-6}	20	1.5 K	Yes	47
GaAs/AlGaAs	1.0×10^{-4}	0.04	2.5×10^{-6}	3.3	77 K	Yes	48
Si/SiGe	80	0.27	0.296	5.45	300 K	No	49
CaF_2/CdF_2	0.63	1.1	0.001	10^5	300 K	No	50
SiGe/Si	-	1.15	-	7.6	300 K	No	51
GaAs/InGaAs/GaAs	2.5	1.1	0.002	56	300 K	No	52
ML Gr/4L hBN/ML Gr	0.35	0.9	3.9×10^{-4}	2	2 K	Yes	10
ML Gr/5L hBN/ML Gr	0.18	0.45	4.0×10^{-4}	3.5	7 K	Yes	9
BL Gr/2L hBN/BL Gr	0.8	0.29	0.003	2.5	300 K	Yes	13
BL Gr/4L hBN/BL Gr	3.0×10^{-4}	0.14	2.1×10^{-6}	1.5	300 K	Yes	13
BL Gr/5L hBN/BL Gr	3.0×10^{-4}	0.13	2.3×10^{-6}	1.8	300 K	Yes	11
BL Gr/2L WSe_2/BL Gr	**2**	**0.08**	**0.025**	**3.9**	**300 K**	**Yes**	**-**
BL Gr/2L WSe_2/BL Gr	**2.5**	**0.09**	**0.028**	**5.8**	**1.5 K**	**Yes**	**-**

Table 4.1: Comparison of epitaxial and vdW resonant tunneling heterostructures

Chapter 5: Theoretical Modeling of Resonant Tunneling

MODEL

To better understand the physics involved in the experimental tunneling characteristics, we model the ITFET using a perturbative tunneling Hamiltonian.[53,54] The band structures of the top $[\epsilon_{\mathrm{TL}}(k)]$ and bottom $[\epsilon_{\mathrm{BL}}(k)]$ bilayers are computed using a simplified tight-binding model to the leading order in wave-vector k around the **K**-point.[55] The band openings in the top and bottom bilayers are self-consistently estimated by computing the local electric fields in the bilayers, after taking electron screening into consideration.[56]

The electrostatic potential and band alignment of each graphene bilayer is computed using the following set of charge-balance equations

$$C_{\mathrm{IL}}\left(-\frac{\phi_{\mathrm{TL}}}{e}+\frac{\phi_{\mathrm{BL}}}{e}\right)-C_{\mathrm{TG}}\left(V_{\mathrm{TG}}+\frac{\phi_{\mathrm{TL}}}{e}\right)=Q_{\mathrm{TL}}(\epsilon_{\mathrm{TL}},\mu_{\mathrm{TL}},\phi_{\mathrm{TL}}) \tag{5.1}$$

$$C_{\mathrm{IL}}\left(\frac{\phi_{\mathrm{TL}}}{e}-\frac{\phi_{\mathrm{BL}}}{e}\right)-C_{\mathrm{BG}}\left(V_{\mathrm{BG}}+\frac{\phi_{\mathrm{BL}}}{e}\right)=Q_{\mathrm{BL}}(\epsilon_{\mathrm{BL}},\mu_{\mathrm{BL}},\phi_{\mathrm{TL}}) \tag{5.2}$$

where C_{IL} is the interlayer capacitances per unit area, and Q_{TL} (Q_{BL}) is the top (bottom) layer charge density.

The single particle tunneling current between the two bilayer graphene is given by

$$I_{\mathrm{int}}=-e\int_{-\infty}^{\infty}T(E)\big(f(E-\mu_{\mathrm{TL}})-f(E-\mu_{\mathrm{BL}})\big)dE \tag{5.3}$$

where $f(E)$ is the Fermi distribution function. $T(E)$ is the vertical transmission rate of an electron at energy E [57,58]:

$$T(E) = \frac{2\pi}{\hbar} \sum_{k;ss'} |t|^2 A_{\mathrm{TL},s}(k,E) A_{\mathrm{BL},s'}(k,E) \tag{5.4}$$

The interlayer coupling t is modeled as independent of E and k of the graphene bilayers for simplicity. The summation is performed over all momentum states k and the first two conduction and valence sub-bands, denoted by s and s'. $A_{\mathrm{TL},s}$ and $A_{\mathrm{BL},s}$ are the spectral density functions of the band s in the top and the bottom bilayers, respectively. The spectral densities are taken to be Lorentzian in form, i.e.,

$$A_s(k,E) = \frac{1}{\pi} \frac{\Gamma}{(E - \epsilon_s(k))^2 + \Gamma^2} \,, \tag{5.5}$$

where Γ represents the energy broadening half-width of the quasi-particle states, and $\epsilon_s(k)$ is the energy dispersion of band s at wave-vector k. We note that Γ may also contain contributions from the spatial variation in the electrostatic potential difference between layers due to disorder.

The only free parameters in this model are the interlayer coupling t and energy broadening parameter Γ. The bilayers are assumed to be rotationally aligned. A rotation between the bilayers would be expected to increase the broadening for small angles, and then entirely eliminate resonant tunneling at larger angles.[15] Figure 5.1a and 4.1b compare I_{int} vs. ΔV calculated according to our model, to the experimental data of Figure 4.4a and 3.4b, measured at T = 300 K, and T = 1.5 K, respectively. To best fit the experimental data of Figure 4.4a and 3.4b, we use an energy broadening Γ = 6 meV at T = 300 K, and Γ = 4 meV at T = 1.5 K, and an interlayer coupling $|t|$ = 30 μeV.

To provide additional understanding, we perform *ab initio* density functional theory (DFT) simulations for the bilayer graphene – bilayer WSe_2 – bilayer graphene system. The

supercell structures are relaxed using the projector-augmented wave method with a plane wave basis set as executed in the Vienna *ab initio* simulation package (VASP).[59,60] The square of the interlayer coupling is proportional to the interlayer tunneling current within a first-order approximation. The effective interlayer coupling can be estimated from DFT simulations as half of the resonant splitting in the conduction bands at zero electrostatic potential difference between the layers, where the conduction bands of the two layers would be degenerate in the absence of interlayer coupling.[61] Figure 5.1c shows the band structures of a bilayer graphene – bilayer WSe_2 – bilayer graphene heterostructure (solid, black), along with that of a single bilayer graphene (dashed, red) as reference. The relatively large energy splitting between the conduction and valence bands in the vicinity of the **K**-point (inset) is the result of bilayer graphene coupling *to* the WSe_2. The smaller splitting of the conduction and valence bands within the graphene – bilayer WSe_2 – bilayer graphene heterostructures is the result of primary interest, and stems from coupling of the two bilayer graphene to each other *through* the bilayer of WSe_2. This momentum-dependent splitting is larger than 500 μeV near the band edge, and away from the **K**-point remains substantially larger than $2|t|$ = 60 μeV, used in the calculations for Figure 5.1a and 4.1b. Prior theoretical work suggests that rotational misalignment between the graphene bilayers, as well as misalignment of the conductive layers with the interlayer barrier, will substantially reduce both energies.[61] The difference between the coupling determined from the experimental data and the *ab initio* DFT calculations suggests there may be substantial room to further improve the interlayer current.

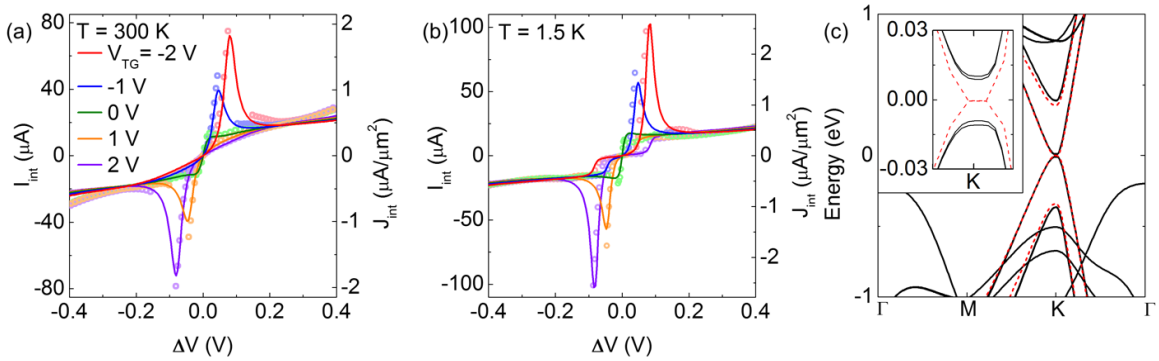

Figure 5.1: Comparison of experimental data with calculations. (a, b) Calculated I_{int} vs. ΔV (solid lines) at different V_{TG}, at (a) T = 300 K and (b) T = 1.5 K. The experimental four-point data are shown as symbols. The model accurately reproduces the experimental findings at both temperatures with an energy broadening half width Γ = 6 meV at T = 300 K, and Γ = 4 meV at T = 1.5 K. (c) Band structures for a bilayer graphene – bilayer WSe_2 – bilayer graphene heterostructure (black solid lines), and bilayer graphene (dashed red lines) obtained from DFT simulations. The relatively large splitting between the conduction and valence bands in the vicinity of the **K**-point (inset) stems from the coupling of bilayer graphene to WSe_2. The smaller splitting of the conduction and valence bands within the graphene – bilayer WSe_2 – bilayer graphene heterostructure stems from coupling of the two bilayers of graphene through the bilayer of WSe_2.

UNLIKE-BAND TUNNELING

It is instructive to examine in further detail key features in the I_{int} vs. ΔV data, and the physical mechanisms explaining these observations. As modeled in Figure 5.2a, at T = 1.5 K, like-band energy and momentum conserving resonant tunneling (i.e. valence to valence band, or conduction to conduction band) accounts for the resonance peak in the I_{int} vs. ΔV, while energy and momentum conserving non-resonant, unlike-band tunneling (e.g., conduction to valence band) produces a background tunneling current when the energy-momentum ring of intersection between unlike bands falls between the layer chemical potentials. Figure 5.2b shows different band alignments schematically, and the conditions leading to these different tunneling regimes, where each panel (1-6) refers to the labeled point in Figure 5.2a and a corresponding voltage $V_{1\text{-}6}$. At $\Delta V = V_1$, the current is dominated

by unlike-band tunneling. In this regime of operation, the current depends on the joint density of states at the ring of intersection and not on the magnitude of ΔV. As ΔV increases towards V_2, the ring of intersection moves outside the chemical potential difference and thereby causes a dip in the current. For the same reason, there are no states that contribute to the energy and momentum conserving current as the voltage is increased to V_3 and V_4. At $\Delta V = V_5$, the band structures of the top and bottom layers align, resulting in a large resonant current, which predominantly comes from like-band tunneling between the top and bottom layer valence bands in this case. As such, the current at resonance increases with ΔV. Finally, as the voltage is further increased to $\Delta V = V_6$, energy and momentum conserving current from the top layer conduction band to bottom layer valence band takes over as the dominant source of tunneling current, with the current again dependent only on the joint density of states at the ring of intersection.

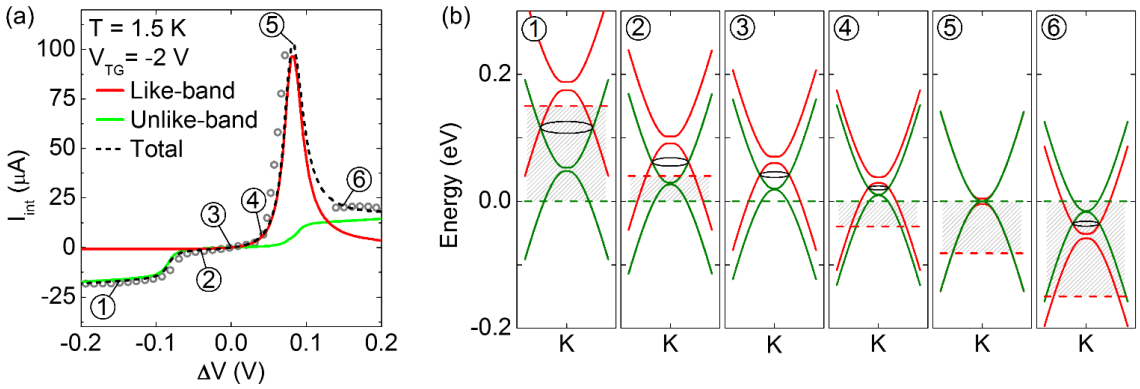

Figure 5.2: Different contributions to the total interlayer tunneling current. (a) Calculated I_{int} vs. ΔV at V_{TG} = -2 V and T = 1.5 K. The simulated data shows the total interlayer tunneling current (black), along with the like- (red) and unlike-band (green) tunneling. The corresponding experimental data (symbols) are included for comparison. (b) Energy band-alignment of the top (red) and bottom (green) graphene bilayers at various bias voltages. The tunneling current between the unlike bands flows through the tunnel barrier when the momentum conserving ring of overlap (black) lies within the chemical potential difference. Resonant tunneling current between like bands flows when the band structures completely align at $\Delta V = V_5$.

Another way of elucidating the unlike-band tunneling behavior is by considering the differential conductance as a function of both V_{TG} and ΔV. In this representation, the onset of unlike-band tunneling at positive and negative ΔV, which occurs when the ring of intersection is at the Fermi level of one of the layers, creates peaks in the conductance data that accompany the large peak at resonance. By observing the behavior of these secondary peaks, additional insight can be gained. Figure 5.3 shows theoretical and experimental contour plots of the differential conductance as a function of V_{TG} and ΔV. The resonance peak, shown by the line of high g_{int} coupled with a line of negative g_{int}, is clearly visible and is flanked by the two smaller unlike-band tunneling peaks, which form an 'X' pattern. The positive and negative slopes of the unlike-band tunneling peaks match that of resonance, further confirming their origin as stemming from band alignments driven by gate and interlayer biases. Additionally, information on the relative carrier densities in the two layers can be inferred from the unlike-band tunneling peaks. Namely, at the vertex of 'X' pattern, the ring of intersection must align with the Fermi level of both layers simultaneously, meaning the carrier densities in each layer are equal and opposite.

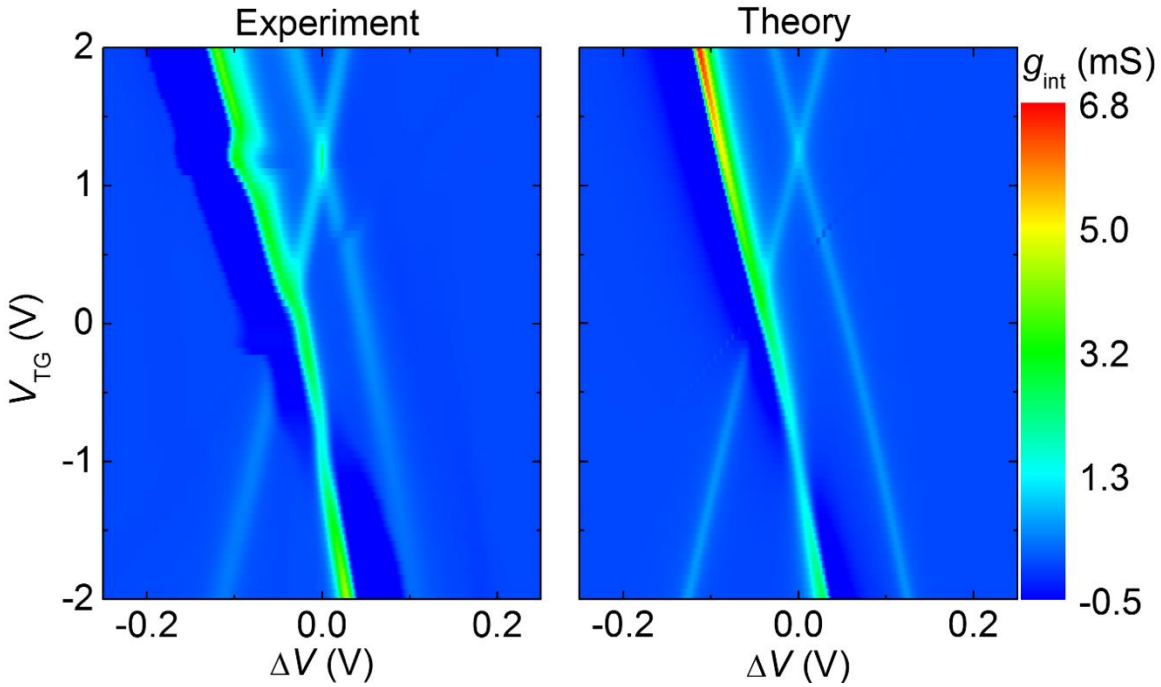

Figure 5.3: Measured and calculated differential tunneling conductance as a function ΔV and V_{TG} at V_{BG} = 20 V. The single line of high conductance corresponds to the resonance peak, and the two additional lines of moderate conductance forming an 'X' pattern correspond to the onset of unlike-band tunneling with increasing ΔV.

The clearly defined regions of unlike-band tunneling are less prominent as temperature increases due to the spread of the Fermi distribution, which allows tunneling between the top and bottom bilayers even when the momentum and energy conserving ring of intersection lies outside the chemical potential difference window. Furthermore, at 300 K, an additional current component appears, as shown by the small difference between the theoretical and experimental curves at large interlayer bias in Figure 5.1a, suggesting a phonon-induced momentum-randomizing interlayer current between like or unlike bands. The addition of phonon scattering is qualitatively consistent with the increased broadening at 300 K. However, the predominant source of interlayer current, even off resonance, remains energy and momentum conserving tunneling (within the broadening), either

resonant or non-resonant. Given the excellent agreement between the modeled and experimental results, the data of Figure 5.1 suggest that energy and momentum conserving coherent tunneling is the dominant source of current at all interlayer biases in the experimental data at 1.5 K, a strong indication of layer-to-layer alignment, and high-quality interfaces within the heterostructure.

Chapter 6: Summary

In summary, a comprehensive overview of resonant tunneling heterostructures consisting of double bilayer graphene separated by bilayer WSe_2 and encapsulated in hBN has been presented. The basic introduction to the electronic properties of two-dimensional materials outlined in Chapter 2 provides a groundwork and motivation for pursuing resonant tunneling in two-dimensional heterostructures, in which carriers can tunnel between two rotationally aligned graphene layers while conserving energy and momentum.

While the concept of resonant tunneling is straightforward, building a heterostructure to demonstrate the effect is challenging. Chapter 3 describes the approaches used to create resonant tunneling heterostructures, which requires thoughtful design of the heterostructures, careful selection of initial layers, precise alignment of layers during transfers, and frequent annealing to maintain good layer adhesion and cleanliness. The large number of steps and points of failure make the fabrication of a resonant tunneling heterostructure a success in and of itself.

In Chapter 4 and Chapter 5 we demonstrate experimentally and model theoretically gate-tunable resonant tunneling and negative differential resistance in bilayer graphene – bilayer WSe_2 – bilayer graphene heterostructures. The interlayer current-voltage characteristics show current densities reaching 2 $\mu A/\mu m^2$ and 2.5 $\mu A/\mu m^2$, and PVRs of 4 and 6, at T = 300 K and 1.5 K, respectively. These values coupled with narrow resonant conductance peaks suggest that heterostructures realized using layer-by-layer transfers can be of comparable quality to that of epitaxial heterostructures. The excellent agreement between theoretical calculations and experimental data indicates that the interlayer current stems primarily from energy and momentum conserving, coherent 2D-2D tunneling with non-momentum conserving tunneling negligible at 1.5 K, and relatively small at 300K. We

observe narrow tunneling resonances, with intrinsic half-widths of 4 and 6 meV at 1.5 K and 300 K, respectively.

References

1. Geim, A. K. & Grigorieva, I. V. Van der Waals heterostructures. *Nature* **499**, 419–425 (2013).
2. Dean, C. R. *et al.* Boron nitride substrates for high-quality graphene electronics. *Nat. Nanotechnol.* **5**, 722–726 (2010).
3. Ponomarenko, L. A. *et al.* Cloning of Dirac fermions in graphene superlattices. *Nature* **497**, 594–597 (2013).
4. Dean, C. R. *et al.* Hofstadter's butterfly and the fractal quantum Hall effect in moire superlattices. *Nature* **497**, 598–602 (2013).
5. Hunt, B. *et al.* Massive Dirac Fermions and Hofstadter Butterfly in a van der Waals Heterostructure. *Science* **340**, 1427–1430 (2013).
6. Woods, C. R. *et al.* Commensurate-incommensurate transition in graphene on hexagonal boron nitride. *Nat. Phys.* **10**, 451–456 (2014).
7. Fallahazad, B. *et al.* Shubnikov--de Haas Oscillations of High-Mobility Holes in Monolayer and Bilayer WSe_2: Landau Level Degeneracy, Effective Mass, and Negative Compressibility. *Phys. Rev. Lett.* **116**, 086601 (2016).
8. Cui, X. *et al.* Multi-terminal transport measurements of MoS_2 using a van der Waals heterostructure device platform. *Nat. Nanotechnol.* **10**, 534–540 (2015).
9. Britnell, L. *et al.* Resonant tunnelling and negative differential conductance in graphene transistors. *Nat. Commun.* **4**, 1794 (2013).
10. Mishchenko, A. *et al.* Twist-controlled resonant tunnelling in graphene/boron nitride/graphene heterostructures. *Nat. Nanotechnol.* **9**, 808–813 (2014).
11. Fallahazad, B. *et al.* Gate-Tunable Resonant Tunneling in Double Bilayer Graphene Heterostructures. *Nano Lett.* **15**, 428–433 (2015).
12. Kang, S. *et al.* Bilayer Graphene-Hexagonal Boron Nitride Heterostructure Negative Differential Resistance Interlayer Tunnel FET. *IEEE Electron Device Lett.* **36**, 405–407 (2015).
13. Kim, K. *et al.* van der Waals Heterostructures with High Accuracy Rotational Alignment. *Nano Lett.* **16**, 1989–1995 (2016).
14. Wallbank, J. R. *et al.* Tuning the valley and chiral quantum state of Dirac electrons in van der Waals heterostructures. *Science* **353**, 575–579 (2016).
15. Feenstra, R. M., Jena, D. & Gu, G. Single-particle tunneling in doped graphene-insulator-graphene junctions. *J. Appl. Phys.* **111**, 043711 (2012).
16. Zhao, P., Feenstra, R. M., Gu, G. & Jena, D. SymFET: A Proposed Symmetric Graphene Tunneling Field-Effect Transistor. *IEEE Trans. Electron Devices* **60**, 951–957 (2013).
17. Banerjee, S. K., Register, L. F., Tutuc, E., Reddy, D. & MacDonald, A. H. Bilayer

PseudoSpin Field-Effect Transistor (BiSFET): A Proposed New Logic Device. *IEEE Electron Device Lett.* **30**, 158–160 (2009).
18. Sedighi, B., Hu, X. S., Nahas, J. J. & Niemier, M. Nontraditional Computation Using Beyond-CMOS Tunneling Devices. *IEEE J. Emerg. Sel. Top. Circuits Syst.* **4**, 438–449 (2014).
19. Novoselov, K. S. *et al.* Electric Field Effect in Atomically Thin Carbon Films. *Science* **306**, 666–669 (2004).
20. Zhang, Y., Tan, Y.-W., Stormer, H. L. & Kim, P. Experimental observation of the quantum Hall effect and Berry's phase in graphene. *Nature* **438**, 201–204 (2005).
21. Observation of the fractional quantum Hall effect in graphene | Nature. Available at: https://www.nature.com/articles/nature08582. (Accessed: 20th November 2018)
22. Zhang, Y. *et al.* Direct observation of a widely tunable bandgap in bilayer graphene. *Nature* **459**, 820–823 (2009).
23. Wang, Q. H., Kalantar-Zadeh, K., Kis, A., Coleman, J. N. & Strano, M. S. Electronics and optoelectronics of two-dimensional transition metal dichalcogenides. *Nat. Nanotechnol.* **7**, 699–712 (2012).
24. Watanabe, K., Taniguchi, T. & Kanda, H. Direct-bandgap properties and evidence for ultraviolet lasing of hexagonal boron nitride single crystal. *Nat. Mater.* **3**, 404–409 (2004).
25. Lee, C.-H. *et al.* Atomically thin p–n junctions with van der Waals heterointerfaces. *Nat. Nanotechnol.* **9**, 676–681 (2014).
26. Black Phosphorus–Monolayer MoS_2 van der Waals Heterojunction p–n Diode - ACS Nano (ACS Publications). Available at: https://pubs.acs.org/doi/abs/10.1021/nn5027388. (Accessed: 20th November 2018)
27. Britnell, L. *et al.* Strong Light-Matter Interactions in Heterostructures of Atomically Thin Films. *Science* **340**, 1311–1314 (2013).
28. Yu, W. J. *et al.* Highly efficient gate-tunable photocurrent generation in vertical heterostructures of layered materials. *Nat. Nanotechnol.* **8**, 952–958 (2013).
29. Britnell, L. *et al.* Field-Effect Tunneling Transistor Based on Vertical Graphene Heterostructures. *Science* **335**, 947–950 (2012).
30. Georgiou, T. *et al.* Vertical field-effect transistor based on graphene-WS_2 heterostructures for flexible and transparent electronics. *Nat. Nanotechnol.* **8**, 100–103 (2013).
31. Burg, G. W. *et al.* Coherent Interlayer Tunneling and Negative Differential Resistance with High Current Density in Double Bilayer Graphene–WSe2 Heterostructures. *Nano Lett.* **17**, 3919–3925 (2017).
32. Wang, L. *et al.* One-Dimensional Electrical Contact to a Two-Dimensional Material. *Science* **342**, 614–617 (2013).

33. Ferrari, A. C. *et al.* Raman Spectrum of Graphene and Graphene Layers. *Phys. Rev. Lett.* **97**, 187401 (2006).
34. Terrones, H. *et al.* New First Order Raman-active Modes in Few Layered Transition Metal Dichalcogenides. *Sci. Rep.* **4**, 4215 (2014).
35. Kang, S. *et al.* Effects of Electrode Layer Band Structure on the Performance of Multilayer Graphene–hBN–Graphene Interlayer Tunnel Field Effect Transistors. *Nano Lett.* **16**, 4975–4981 (2016).
36. Shi, Y. *et al.* Synthesis of Few-Layer Hexagonal Boron Nitride Thin Film by Chemical Vapor Deposition. *Nano Lett.* **10**, 4134–4139 (2010).
37. Kim, K. K. *et al.* Synthesis of Monolayer Hexagonal Boron Nitride on Cu Foil Using Chemical Vapor Deposition. *Nano Lett.* **12**, 161–166 (2012).
38. Kam, K. K. & Parkinson, B. A. Detailed photocurrent spectroscopy of the semiconducting group VIB transition metal dichalcogenides. *J. Phys. Chem.* **86**, 463–467 (1982).
39. Zhang, C. *et al.* Probing Critical Point Energies of Transition Metal Dichalcogenides: Surprising Indirect Gap of Single Layer WSe2. *Nano Lett.* **15**, 6494–6500 (2015).
40. Fallahazad, B. *et al.* Shubnikov de Haas Oscillations of High-Mobility Holes in Monolayer and Bilayer WSe_2: Landau Level Degeneracy, Effective Mass, and Negative Compressibility. *Phys. Rev. Lett.* **116**, 086601 (2016).
41. Kim, K. *et al.* Band Alignment in WSe2–Graphene Heterostructures. *ACS Nano* **9**, 4527–4532 (2015).
42. Huang, C. I. *et al.* AlGaAs/GaAs double barrier diodes with high peak-to-valley current ratio. *Appl. Phys. Lett.* **51**, 121–123 (1987).
43. Söderström, J. R., Chow, D. H. & McGill, T. C. New negative differential resistance device based on resonant interband tunneling. *Appl. Phys. Lett.* **55**, 1094–1096 (1989).
44. Smet, J. H., Broekaert, T. P. E. & Fonstad, C. G. Peak-to-valley current ratios as high as 50:1 at room temperature in pseudomorphic In0.53Ga0.47As/AlAs/InAs resonant tunneling diodes. *J. Appl. Phys.* **71**, 2475–2477 (1992).
45. Brown, E. R. *et al.* Oscillations up to 712 GHz in InAs/AlSb resonant-tunneling diodes. *Appl. Phys. Lett.* **58**, 2291–2293 (1991).
46. Day, D. J., Yang, R. Q., Lu, J. & Xu, J. M. Experimental demonstration of resonant interband tunnel diode with room temperature peak-to-valley current ratio over 100. *J. Appl. Phys.* **73**, 1542–1544 (1993).
47. Blount, M. A. *et al.* Double electron layer tunnelling transistor (DELTT). *Semicond. Sci. Technol.* **13**, A180 (1998).
48. Simmons, J. A. *et al.* Planar quantum transistor based on 2D–2D tunneling in double quantum well heterostructures. *J. Appl. Phys.* **84**, 5626–5634 (1998).
49. Duschl, R., Schmidt, O. G. & Eberl, K. Epitaxially grown Si/SiGe interband tunneling

diodes with high room-temperature peak-to-valley ratio. *Appl. Phys. Lett.* **76**, 879–881 (2000).
50. Watanabe, M., Funayama, T., Teraji, T. & Sakamaki, N. CaF2/CdF2 Double-Barrier Resonant Tunneling Diode with High Room-Temperature Peak-to-Valley Ratio. *Jpn. J. Appl. Phys.* **39**, L716 (2000).
51. Suda, Y. & Koyama, H. Electron resonant tunneling with a high peak-to-valley ratio at room temperature in Si1−xGex/Si triple barrier diodes. *Appl. Phys. Lett.* **79**, 2273–2275 (2001).
52. Rommel, S. L. *et al.* Record PVCR GaAs-based tunnel diodes fabricated on Si substrates using aspect ratio trapping. in *2008 IEEE International Electron Devices Meeting* 1–4 (2008). doi:10.1109/IEDM.2008.4796801
53. Zheng, L. & MacDonald, A. H. Tunneling conductance between parallel two-dimensional electron systems. *Phys. Rev. B* **47**, 10619–10624 (1993).
54. Turner, N. *et al.* Tunneling between parallel two-dimensional electron gases. *Phys. Rev. B* **54**, 10614–10624 (1996).
55. Castro Neto, A. H., Guinea, F., Peres, N. M. R., Novoselov, K. S. & Geim, A. K. The electronic properties of graphene. *Rev. Mod. Phys.* **81**, 109–162 (2009).
56. Min, H., Sahu, B., Banerjee, S. K. & MacDonald, A. H. Ab initio theory of gate induced gaps in graphene bilayers. *Phys. Rev. B* **75**, 155115 (2007).
57. Bardeen, J. Tunnelling from a Many-Particle Point of View. *Phys. Rev. Lett.* **6**, 57–59 (1961).
58. Barrera, S. C. de la, Gao, Q. & Feenstra, R. M. Theory of graphene–insulator–graphene tunnel junctions. *J. Vac. Sci. Technol. B* **32**, 04E101 (2014).
59. Kresse, G. & Furthmüller, J. Efficient iterative schemes for \textit{ab initio} total-energy calculations using a plane-wave basis set. *Phys. Rev. B* **54**, 11169–11186 (1996).
60. Kresse, G. & Furthmüller, J. Efficiency of ab-initio total energy calculations for metals and semiconductors using a plane-wave basis set. *Comput. Mater. Sci.* **6**, 15–50 (1996).
61. Valsaraj, A., Register, L. F., Tutuc, E. & Banerjee, S. K. DFT simulations of inter-graphene-layer coupling with rotationally misaligned hBN tunnel barriers in graphene/hBN/graphene tunnel FETs. *J. Appl. Phys.* **120**, 134310 (2016).